Turbulence Measurements on a 2D NACA 0036 with Synthetic Jet Flow Control

J. S. Wilson*
University Affiliated Research Center (UARC)
University of California Santa Cruz
Ames Research Center, Moffett Field, CA

An active flow control experiment was conducted on a 2-ft chord NACA 0036 airfoil in a 3-ft by 4-ft Wind Tunnel at $Re = 1.0 \times 10^6$. The model was equipped with synthetic jet actuators at x/c = 0.30 and 0.65 that provided 120 Hz periodic excitation at a $C_\mu = 0.86\%$ through 0.06-in wide slots. Three different slot configurations were tested, including a baseline with no slots. Surface pressure data was collected to compare to previous tests and to combine with turbulence data to aid future CFD modeling efforts. Turbulence data, measured by hot-wire, was compared with and without flow control. Pressure data corroborates previous test data and provides more points for CFD validation. Hot-wire results showed flow control reduced the separated wake size and brought the high Reynolds stress shear layer closer to the airfoil surface. The position of this layer to the surface was altered more significantly than the magnitude of the peak stresses. Flow control was shown to increase turbulent energy in the attached boundary layer downstream of the slot but to have little effect upstream. These results provide further justification to continue assessing the potential of active flow control to reduce drag of helicopter airframe components.

Nomenclature

C_a	Axial force coefficient
C_d	Pressure Drag coefficient
C_l	Lift coefficient
C_n	Normal force coefficient
C_p	Pressure coefficient
C_μ	Actuator momentum coefficient, $hV_{jet}{}^2 / \left(U_\infty{}^2 c\right)$
c	Airfoil chord, ft
$F+$	Non-dimensional frequency, $fc(1 - \frac{x_s}{c})/U_\infty$
f	Flow control actuator frequency, Hz
h	Width of actuator slot exit, in
q	Freestream dynamic pressure, lbs/ft^2
Re	Reynolds number based on chord
U_∞	Freestream velocity, ft/s
$\overline{u}$	Time averaged streamwise component of velocity
$\overline{u'v'}$	Reynolds shear stress
$\overline{V}$	Time averaged total velocity
$\overline{v}$	Time averaged vertical component of velocity
V_{jet}	Peak velocity at actuator slot exit, ft/s
$\overline{V'V'}$	Total velocity normal stress
x	Chordwise position or traverse coordinate
x_s	Actuator slot location from leading edge
y	Distance from model surface or traverse coordinate
α	Angle of attack, deg
δ	Boundary layer thickness
δ_w	Wake thickness at trailing edge

Introduction

A primary source of cruise drag and download on a helicopter is bluff-body drag. Structures such as pylons, rotor hubs, and fuselages are usually thick shapes aerodynamically optimized for a single flight condition. These structures can experience considerable separated flow and create large amounts of drag or download. Additionally, yawed flight, gusts, and maneuvers can increase the apparent angle of attack on various structures, further aggravating separation. The large wakes generated by separation can add another dimension by increasing interference drag. These features of helicopters make postponement of flow separation a key area for drag and download reduction and thus improved performance (Refs. 1, 2, 3). Active flow control (AFC) by synthetic jets has the potential to provide this postponement of flow separation. Figure 1 illustrates the potential performance improvement. If AFC is applied to drag and download reduction there is a large increase in available payload for long range missions.

Turbulent Flow Separation

Flow separation over a surface occurs because of momentum loss in the boundary layer. Adverse pressure gradients caused from the surface curvature of bluff bodies is a major source of this momentum loss. As momentum is lost, the velocity profile becomes vertical near the surface, and the shear stress diminishes. At some point, the shear stress and velocity simultaneously vanish at a point within the boundary layer. When this happens, the boundary layer separates from the surface. The separated boundary layer then either reattaches somewhere downstream forming a separation bubble or stays detached outlining a wake region. In order to delay separation, momentum must some how be added to or maintained in the boundary layer.

Flow Control

Numerous methods have been used historically to delay or control separation. Most methods used today in full-scale flight are of the "passive" type, such as vortex

*Research Scientist

generators and streamlining of rotor hubs (Ref. 4). These methods have their own benefits, namely simplicity, and drawbacks, such as being a point design.

Two traditional forms of active flow control (AFC) are steady suction and blowing. These two methods either remove low momentum flow by suction or add momentum by blowing in the boundary layer. For example, a suction slot could be positioned within a separation bubble and pull away the low speed fluid. A blowing slot angled to the surface could expel high-momentum fluid directly into the lower region of a boundary layer where momentum was lost (Ref. 5). Over the years many wind tunnel experiments have shown that these traditional methods improve performance, but the weight, complexity, and power required by these systems generally outweigh any benefits for full scale aircraft. Another type of flow control that has gained popularity, partially because of the drawbacks of traditional methods, is periodic excitation (Ref. 6).

Periodic excitation has its roots in the early experiments to initiate Tollmien-Shlichting waves by acoustic excitation. Periodically applying either suction or blowing alone has since become a branch of periodic excitation methods for flow control. This method is classified as "net-mass flux" because over a cycle mass is either being taken away or added to the flow. Periodic net-mass flux systems have been shown to be effective with a momentum addition to the flow one or two orders of magnitude less than that of steady suction or blowing. This greatly reduces the power required to operate such a system, however the complexity of generating and transferring that net-mass flux to the flow remains a challenge.

In contrast, "zero net-mass flux" actuators draw in a low-momentum mass of fluid and expel an equal mass of high-momentum fluid. Thus no mass is being supplied or taken away, yet momentum is being added to the flow. In quiescent air this suction and blowing action creates a pair of counter rotating vortices, where between these vortices an outward velocity is induced. This region of mean outward flow is termed the synthetic jet. In a boundary layer flow, these vortices not only act as a momentum pump but also enhance turbulent mixing between the slower fluid and the freestream. A schematic of a synthetic jet actuator embedded in a surface is shown in Fig. 2. These synthetic jet actuators can be independent of propulsion systems and only require electrical power, reducing the drawbacks of earlier systems (Ref. 6).

The two main controlling parameters of a synthetic jet are its excitation frequency and momentum output. These parameters are typically quantified by the non-dimensional frequency, $F+$, and momentum coefficient, C_μ. Data indicates that the effective ranges of these parameters are approximately $0.3 \leq F+ \leq 4$ and $0.01\% \leq C_\mu \leq 3.0\%$ (Ref. 6).

Previous Work

Active flow control has recently been applied to rotor blade dynamic stall, aft fuselage upsweep, and download issues associated with tilt-rotor aircraft (Refs. 7, 8).

Previous work by the Army AFDD and Israeli Ministry of Defense aimed to extend active flow control technology to drag reduction on a thick pylon-like airfoil representative of geometry on many vehicles (Ref. 2). After a series of flow visualization experiments, a 2-D NACA 0036 active separation control model with synthetic jet actuators was built. Airfoil pressure distributions and wake velocity surveys were used to analyze AFC effectiveness at angles of attack from 0 to 10 degrees in varying actuator configurations. The AFC system was able to delay separation and reduce wake size over a wide range of angles. The results illustrated the importance of having the flow control slot upstream of the separation location; however, little could be gathered about the flow physics from the data acquired. A blind CFD comparison using a RANS code showed trends opposite that of the experimental results. In addition, no significant separation control was predicted. When turbulent kinetic energy (TKE) was plotted from CFD data, there was no change detected between the baseline and $x/c = 0.30$ slot case with $C_\mu = 0.4\%$. The CFD $x/c = 0.65$ slot case, $C_\mu = 0.4\%$, showed a significant difference in the TKE distribution from the baseline but did not predict a change in pressure distribution. It was concluded that more flow field data was needed to improve the turbulence model.

Goals of Current Experiment

It had been shown that the 2D NACA 0036 active flow control system can delay separation, reduce wake size and improve performance. CFD analysis had not been able to predict this observed behavior. The study reported here is meant to build on the previous work by providing corroborating pressure data and new detailed turbulence data. This turbulence data is critical to selecting and maturing a turbulence model for predicting and designing flow control systems.

Test Description

Although an existing wind tunnel was used in this experiment, a significant new investment in turbulence measurement and active flow control research capability was produced by the author for this project.

Wind Tunnel Facility

The experiment was conducted in the California Polytechnic State University San Luis Obispo (CPSU) 3-ft by 4-ft low-speed, open return, wind tunnel shown below in Fig. 3. A 150 hp, 440 Volt three-phase motor powered a nine-blade suction fan. The tunnel inlet had an 11:1 contraction with a flow straightening section followed by three screens at the entrance. Upstream segments of the test section were refurbished before this experiment to further improve flow quality. The variation in mean velocity is less than 1% and the freestream turbulence intensity is less than 0.5% over the center three fourths of the tunnel cross section. A calibrated pressure ring system installed across the contraction section was used to measure tunnel speed.

Low Vibration Test Section

A new test section, with integral traverse and probe support, was designed and built for this experiment. The large flow separation in this particular experiment can result in significant vibrations of the tunnel. These vibrations can then physically vibrate the hot-wire through the support structure and produce large signal noise. To negate this problem a structurally rigid test section is needed. The new test section was designed using extruded aluminum parts, assembled at the Army AFDD facilities at Moffett Field California, and then shipped to CPSU. The new test section is shown in the different construction phases in Fig. 4.

This new test section has 0.50-in.-thick Lexan side walls, with its ceiling and floor made of high-grade plywood. A 2-in slot bisects one wall of the tunnel, which allows a probe to be inserted into the tunnel. The slot is sealed with a top and a bottom layer of plastic foam while overlapping rubber flashing adds extra strength to the seal from the outside. This seal prevents air leakage while still allowing the probe to move between the top and bottom layers. The plastic foam also acts as a damper to any vibrations of the probe support.

The test section is designed to incorporate Cal Poly's TSI T-2D traverse, shown in Fig. 3. Each of the two axes has an accuracy of 0.0118 in and a repeatability of 0.0004 in. An Isel Automation C142-4.1 Microstep Controller takes commands from the controlling PC through a RS232 interface and runs the traverse. Side rails were built onto the test section to mount the traverse. These rails allow the traverse to move the length of the test section and travel in and out with precision. This greatly simplifies alignment and setup of the traverse and thus the hot-wire probes.

Probe Support

The probe support was designed in a 3-D modeling program and CNC milled. A NACA 0020 airfoil at the root is blended to an Eppler 862 low- Reynolds-number airfoil at the tip to minimize vortex shedding (Fig. 5). The airfoil sections along the support are aligned along their quarter chord to minimize any aeroelastic problems. The probe support is made of upper and lower halves. Hot-wire probe stems and thermocouples are placed between these two halves in guide channels and electrically isolated with insulating tape. The two halves are then bolted together and clamped to the traverse. A diagram of the test setup is shown in Fig. 6.

Active Flow Control Model

Figure 7 shows the 2-ft chord NACA 0036 active separation control model. The model attaches to the tunnel floor and spans to the ceiling creating a 2D setup. The model's quarter chord was placed 3.5 chords downstream and 5.5 chords upstream of the test-section's respective inlet and exit to minimize effects on the pressure ring system.

Thirty-four pressure ports were placed around the airfoil at the model's middle plane. Pressure tubing ran out of the bottom of the model and tunnel to a pressure scanner. Roughness strips were applied at $x/c = 0.05$ to force turbulent transition. These strips were made from 3MTM Safety Walk Tape, 1-in wide fine resilient tread which were shown to effectively force transition in the previous experiment (Ref. 2).

Banks of synthetic jet actuators were built into the model at two chord-wise locations on both sides of the model. The actuator cavities were covered with curved plates to create 0.06-in wide exit slots located at chord positions $x/c = 0.30$ and 0.65. A solid baseline plate was put in place when a slot is not desired. A V_{jet} verses input power calibration was conducted before testing and used thereafter to set C_μ. The average "peak" jet velocity was measured with a miniature hot-wire and used in the C_μ equation.

A Pragmatic 2714A 20MS/s waveform generator, with a frequency accuracy of 0.01 Hz, was used to apply an AC signal to the actuators. The driving waveform was sent to a Peavey GPS 3500 power amplifier to boost the input power. This was a professional stereo amplifier with a total harmonic distortion less than 0.1% and a slew rate of 40 V/s. A voltmeter was used to verify the voltage output to the actuators.

Instrumentation

Pressure Measurement

Pressure data are acquired using a Scanivalve ZOC33/64Px-X1 pressure-scanning module. This module has 64 differential pressure ports; 32 ports with a pressure range of 0.36 *psid* and another 32 ports with a range of 1.0 *psid*. The accuracy of all ports was +/- 0.20% full-scale reading. An internal temperature sensor compensates for temperature changes in the module. Before use, the module is simply allowed to reach a constant temperature and then zeroed. A RAD3200 A/D unit amplifies and samples the signal from the pressure scanner and relays the information through a USB hub to the computer software program "RAD" version 2.04.

Hot-wire Anemometry

The improvement of turbulence models requires the most accurate turbulence measurements possible. A hot-wire anemometer was chosen because it is relatively cheap and easy to operate in comparison to a Laser Doppler Anemometer. Particle Imaging Velocimetry could have been used. However, it is questionable as to whether accurate turbulent quantities could be measured due to spatial resolution and particle seeding issues in zones of large flow separation.

A TSI IFA300 constant-temperature hot-wire anemometer system was used in this experiment. The IFA 300 system operating functions such as signal conditioning settings and overheat ratios, are controlled by computer software through a RS232 connection. The system also has a built in T-Type thermocouple system for temperature measurement and compensation. Analog hot-wire voltage signals are output to the computer's A/D converter for sampling.

A TSI Model 1129 Automatic Calibrator was used for all hot-wire calibrations. This system works in conjunc-

tion with the IFA300 and computer software to automate the calibration process. Calibration velocities are calculated from compressible gas equations using differential pressure, barometric pressure, temperature, and gas constants. The pressure transducer output is run through the IFA300 signal conditioner and is read by the computer A/D card along with hot-wire and thermocouple outputs. DANTEC 55R53 fiber-film probes were used for all two-component, "x-wire" flow measurements. These probes have a quartz-coated nickel sensor, 1.25 mm long and 70 μm in diameter. The frequency response was found to be 20.24 kHz at 82 ft/s (corresponding to $Re = 1.0 \times 10^6$) by a square wave test.

Boundary layer data was obtained with a DANTEC 55R53 platinum-plated tungsten straight single-wire sensor. The sensor is 1.25 mm long and 15 μm in diameter. The frequency response was not measured experimentally but is cited to be 150 kHz in a mean velocity of 328 ft/s. A DANTEC 55P11 miniature straight single-wire sensor was used for calibration of actuator jet velocity. The small size of this probe allows it to be positioned inside the actuator slot. This probe has a 1.25 mm sensor length, a 5 μm diameter, and a quoted frequency response of 90 kHz at 328 ft/s. Temperature measurement and compensation was done by a fast response T-Type thermocouple.

An eight-channel BNC adapter was used to connect output signals from the IFA300 and actuator signal generator to the DAQ system. An eight-channel PowerDAQ-MFS A/D DAQ card installed in the PC was used to digitize inputs. This card has a maximum sample rate of 1 MHz with 12-bit resolution and a maximum range of +/- 5 volts. The digital signals are then handled by TSI Thermal Pro software version 4.6.

Experimental Procedure

Pressure Measurements

Model surface pressure measurements were sampled at a rate of 2 kHz for 30 sec and saved to a data file. A LabVIEW program was then used to average the data, apply static pressure corrections, resolve C_p values, and calculate force coefficients.

Tunnel dynamic pressure was sampled at every hot-wire data point to account for any fluctuation in tunnel velocity. This data was used later to non-dimensionalize flow quantities. A signal from the traverse controller wired to the external trigger of the Scanivalve RAD3200 A/D controlled the sampling. These samples were taken at 2 kHz for 0.125 sec.

Hot-wire Anemometry

Calibration

Hot-wire calibrations were done at the beginning of every test day and when tunnel flow temperature had drifted more than 3 deg Celsius. All x-wire calibrations used 30 data points from 0 to 164 ft/s, weighted toward the lower velocities. For x-wires, both wires were calibrated simultaneously. A fourth-order curve fit was used to define the calibration relationships. Yaw coefficients for each x-wire were found through a constant velocity +/- 30 yaw angle calibration.

Acquisition

The x-wire survey grid had a vertical spacing of 0.04 in with a streamwise spacing varying from 0.2 in near the upstream slot to 2.0 in downstream of the trailing edge. The grid streamwise span is from x/c = 0.28 to 0.60 downstream of the trailing edge. At each streamwise location the grid spanned from approximately 16 in from the tunnel wall to 0.23 in from the model surface. Downstream of the trailing edge the maximum traverse movement set the grid edge. The model surface coordinates were found by first touching a shorting probe connected to the probe stem to the model and recording the position. The difference in dimensions of the shorting probe and hotwires were then used to determine the coordinates. Slightly fewer data points were taken in the wake when AFC was applied to save time. There were approximately 6500 stations per survey. Each station was sampled at 100 kHz for 1.28 sec with a low-pass filter set at 50 kHz. A typical sample grid is shown in Fig. 8. Single-wire boundary layer surveys were conducted at measurement stations upstream and downstream of the x/c = 0.30 slot. Inward traverse commands were issued manually until the mean velocity dropped to approximately 50% of the velocity at the edge of the boundary layer. Samples are taken at 200 kHz for 1.28 sec.

Post-Processing

All analysis of hot-wire measurements was done in post run processing. Signal-conditioned voltages were first deconditioned using the A/D offset and gain. This produced the bridge voltages, which were then corrected for temperature changes. The calibration equation was then applied, converting bridge voltages back to effective velocities. For a single-wire probe, this effective velocity is the measured velocity vector. For an x-wire, which measures two effective velocities, the yaw coefficients were applied to the two-component Jorgenson's equation, producing effective u- and v-components of the planar velocity. Mean values, statistics, and turbulence quantities were then calculated from these components. With the effective velocities analyzed, data point statistics could be calculated.

Momentum Coefficient

The actuator momentum coefficient was found using the DANTEC 55P11 miniature straight single wire in quiescent air. The hot-wire probe was inserted into the center of the slot until the signal became rectified. Then the hotwire signal was sampled at 100 kHz for 0.16 sec. From this data the average peak blowing velocity was calculated and used to specify V_{jet} for the momentum coefficient.

Results and Discussion

Baseline pressure data was taken at α = 0, 5, and 10 deg. All other data, including hot-wire data, was only taken at α = 10 deg. Table 1 summarizes the test configurations and types of data acquired.

Angle of attack for hot-wire measurements was chosen as the highest angle previously tested in order to enhance the differences between uncontrolled and controlled flow. This provides the thickest shear layer, and therefore easiest to measure in terms of spatial resolution. The momentum coefficient was chosen to be as high as possible while minimizing actuator fatigue. All experimental data was obtained at a chord Reynolds number $Re = 1.0 \times 10^6$. This Reynolds number is chosen to be consistent with previous experiments and CFD analysis. The excitation frequency for all flow control cases was $f = 120$ Hz. This provided an $F+ = 2$ on the upstream actuator and $F+ = 1$ on the downstream. Blockage effects are expected to be high, however, CFD analysis efforts can and should model the test section.

Pressure Data

Baseline Flow

It was important to initially verify that the baseline flow behavior was repeatable because previous testing was conducted in a different wind tunnel facility with different instrumentation. Figure 9 shows C_p vs x/c for the current and previous experiment. The current C_p values agree well in terms of the stagnation point. Peak C_p at $\alpha = 0$ and 5 deg are roughly 0.1 lower, and trailing-edge values are approximately 0.1 to 0.15 lower. Previous data shows the separation point moving from $x/c = 0.80$ to $x/c = 0.50$ as angle of attack increases from $\alpha = 0$ to 10 deg whereas the current data shows the location traveling from $x/c = 0.80$ to $x/c = 0.45$. The difference in separation points is most likely the source for observed C_p differences. Much effort was given to reproduce the pressure distribution obtained previously without full success. The separation characteristics were found to be very sensitive to transition strip type and angle of attack. Note that in the current study $Re = 1.0 \times 10^6$, whereas in the previous experiment $Re = 0.9 \times 10^6$. The slight difference in Reynolds numbers, however, was found to have no significant effect on separation. Depending on the estimation method used, the test section blockage during this test can be considered only slightly lower than the previous. Therefore blockage is not thought to be a major source of separation point difference, however it cannot be completely ruled out at this point.

The net effect of the above differences can be seen in Fig. 10 where lift and drag coefficients are graphed versus angle of attack. In the current data, C_l is lower at $\alpha = 5$ and deg due to the slightly earlier separation. Drag is also lower because the airfoil is experiencing more negative normal force at positive angle of attack. This lower normal force thus contributes less to the force in the drag direction. Despite these differences the C_p, C_l and C_d data show adequately similar behavior.

Lift Reversal Phenomenon

A key airfoil behavior reproduced in this test, initially missed by the CFD analysis, is lift reversal. As the airfoil increases in angle of attack, lift initially decreases and then begins to increase again. Figure 11 illustrates the cause of this phenomenon. At $\alpha = 0$ deg there is already a small amount of separation at the trailing edge. As the airfoil is pitched up the separation on the upper surface grows rapidly while on the bottom surface it is suppressed. The separation on the upper surface limits the flow acceleration (lower pressure peak) while flow on the lower surface experiences relatively high acceleration. As α continues to increase a small suction peak is able to form on the upper surface which begins to relieve the negative lift.

Active Flow Control

With the baseline flow behavior established a comparison to AFC cases can be made. Figure 12 shows C_p versus x/c for the baseline and two flow control cases at $\alpha = 10$ deg. With flow control on the forward slot, separation is pushed back from $x/c \approx 0.45$ to 0.55. At this point the flow experiences a relatively mild separation, characterized by the shallow slope of the upper surface pressure distribution curve. The cross over point of the C_p curves is also moved back with an increased peak and base pressure. Introducing flow control into both slots moves separation further back to $x/c = 0.75$, again with corresponding increases in peak suction pressure and base pressure.

Table 2 lists the integrated pressure forces for comparison. With just the forward slot active, lift is changed from negative to positive by a 170% increase. The addition of the rear slot provides further gains for an over 350% increase in lift over the baseline. Drag is reduced by 7.5% and 14% from the baseline using the forward slot and both slots respectively. These drag reductions are small in comparison to the lift increases, and are in fact a direct result of the large increases in normal force. Again from Table. 2, axial force is reduced up to 96% over the baseline however the component of normal force in the drag direction masks this reduction. These integrated pressure forces serve as a correlation opportunity for CFD analysis but the primary result of this work is the hot-wire measurements.

Flow Field Results: Hot-wire Data

Shear layer and Wake

Figure. 13 shows the evolution of the separation region over the model for each case. The separation region thickness is defined as the point where the $\bar{u}$ velocity within the layer has diminished to 99% of the external velocity, measured with a two component hot-wire. In the baseline case the shear layer quickly diverts from the model surface creating a large separation region; $\delta_w = 7.2$ in thick at the trailing edge. The wake can also be seen to move upwards at it leaves the model which is further evidence of the negative lift at positive alpha. With flow control applied on the forward slot the shear layer leaves the surface later and follows the model surface for a short distance before assuming the freestream direction. The wake thickness in this case is only slightly reduced to $\delta_w = 6.0$ in. Flow control on both slots did not change the location where the shear layer first becomes visible but noticeably effected it's evolution from that point. The layer is this case appears as

a slowly growing thick boundary layer for about 25% of the chord before separating. The separation region thickness is further reduced to $\delta_w = 3.1$ inches and now moves downward indicating positive lift.

Reynolds Shear Stress Measurement

Figures 14, 15, and 16 show Reynolds shear stress contours that are non-dimensionalized by density and dynamic pressure for each case. The traverse coordinate data is triangulated using Tecplot in order to generate color contours. Dotted lines represent the shear layer edge found from mean velocity data. The hatched regions represent areas of probable full or intermittent flow reversal. In these areas is not trusted due to the rectification errors associated with hot-wires.

In the baseline case, a shear layer leaves the model surface at approximately $x/c = 0.45$. A region of high Reynolds shear stress is immediately visible and slowly grows in peak magnitude as it travels downstream. The position of the peak Reynolds shear stress maintains an almost constant position relative to the size of the separated region. An area of low Reynolds shear stress from approximately $x/c = 0.66$ to the trailing edge suggests no separation bubble exists in the mean sense. Downstream of the trailing edge higher Reynolds shear stress from the lower surface is show to be impinging into the upper surface flow.

With flow control on the forward slot the high Reynolds shear stress region rapidly becomes a greater portion of the shear layer and remains lower in the layer than the baseline. The peak magnitude reached, however, is only slightly larger. The high stress region from the lower surface is now more balance in the wake with the upper surface flow.

When both slots are active only the upper edge of the high Reynolds shear stress region is visible until approximately $x/c = .80$. Until this point the peak Reynolds shear stress is maintained closer to the surface than the hot-wire can measure. After this point it is seen that the Reynolds shear stress region develops a similar magnitude and thickness as the other control case but the position of the peak stress is even lower in the layer. The upper and lower surface flows do not appear to significantly push into each other and instead extend downstream almost straight back from the trailing edge.

Near Field Measurements

The hot-wire data presented thus far, has not explored the flow into the boundary layer across the upstream actuator. To look at this region, a straight single wire was used to survey the boundary layer upstream and downstream of the $x/c = 0.30$ slot with and without flow control. When no control was applied the solid baseline cover plate was installed. A schematic of this survey is shown in Fig. 17. The center of the $x/c = 0.30$ slot is set as the origin. Survey "A" is 10 slot widths (0.6-in) upstream and survey "B" is 10 widths downstream.

At the bottom of Fig. 17 the measured normal stress is shown for both survey position. The plotted quantity is the normal stress of the total velocity measurement and is an indicator of the flows level of turbulent energy. Upstream there is little difference in the normal stress between these two cases. Downstream the flow control case has altered the stress distribution drastically. There are now two peaks; one at $y/\delta = 0.5$ and the other much larger peak is so close to the wall it cannot be seen. The peak at $y/\delta = 0.5$ is roughly 30% higher than the baseline at that point. At the measurements close to the wall, the flow control case is approximately 70% higher than the baseline case. These large increases in the normal stress indicate that active flow control is successfully increasing turbulent mixing of the free stream and boundary layer. This mixing increases turbulent energy and strengthens the boundary layer against separation.

Hot-wire cooling effects are a well known source of error for near wall measurements. The additional cooling of the model surface can skew velocity measurements to higher values. The measured peaks discussed above are not likely caused by this effect for two reasons. First, the thermal conductivity of the airfoil model material is relatively low (similar to plywood). Second, although not shown in this paper, there was no peak in the $\bar{u}$ velocity profiles. For these reasons it is concluded that the synthetic jet flow control is responsible for the measured peaks.

These results provide a deeper understanding of the flow control slot sensitively observed in previous work. Flow control works best when the separation point is downstream of the slot. When the separation point is upstream of the slot turbulent energy in the boundary layer will not be significantly affected and therefore flow control will be less effective.

Conclusions

A NACA 0036 airfoil, representative of thick aerodynamic shapes found on rotorcraft, was experimentally studied with synthetic jet active flow control applied at different chord locations. Surface pressure measurements and hot-wire flow surveys were taken in order to characterize the flow control's effect on the flow field. The key conclusions of this study are as follows.

1. Although the pressure distributions of previous work could not be exactly duplicated, the general separation behavior, as well as lift and drag trends were repeated. The lift reversal phenomenon was corroborated and stands as a test case for CFD prediction. Lift was increased and drag was decreased when flow control was applied to the $x/c = 0.30$ slot. Further performance improvements were realized with the addition of flow control at the $x/c = 0.65$ slot

2. The size of the separated wake region was quantified and shown to be reduced by active flow control.

3. Active flow control brought the high Reynolds shear stress region closer to the airfoil surface. The closeness of this shear layer to airfoil surface was effected more than the peak shear stress magnitudes.

4. Near field measurements show that the turbulent energy in the boundary layer just upstream of an actuator slot was not significantly affected but downstream there are large increases.

With the completion of this study, a database of pressure and detailed turbulence data is now available for CFD correlation and improvement of turbulence models for thick airfoils. This turbulence data will enable high performance computing design tools to aid in predicting and designing future rotorcraft flow control systems.

Acknowledgments

This work was funded by the Aeroflightdynamics Directorate (AMRDEC) of the US Army Research, Development, and Engineering Command at Ames Research Center. Testing was conducted in the California Polytechnic State University Aerospace Engineering Department Wind Tunnel located in San Luis Obispo California. I would like to thank Dr. Preston B. Martin, Dr. Chee Tung, and Dr. Jin Tso for their advice and guidance throughout this project. I would also like to thank Dan Powell for his support of tunnel operations.

References

[1]Carlson, R.M., "Helicopter Performance-Transportation's Latest Chromosome: The 21st Annual Alexander A. Nikolsky Lecture", *Journal of the American Helicopter Society*, Vol. 47, No. 1, January 2002.

[2]Martin, P.B., Tung, C., Chandrasekhara, M.S., Arad, E., "Active Separation Control: Measurements and Computations for a NACA 0036 Airfoil", AIAA Paper 2003-3516, 21st Applied Aerodynamics Conference, Orlando, FL, June 23-26, 2003.

[3]Martin, P.B., Tung, C., Hassan, A.A., Cerchie, D., Roth, J., "Active Flow Control Measurements and CFD on a Transport Helicopter Fuselage", AHS Paper 2005-0264, 61st American Helicopter Society Forum, Grapevine, TX, June 2nd, 2005.

[4]Martin, D. M., Mort, R. W., Young, L. A., Squires, P. K., "Experimental Investigation of Advanced Hub and Pylon Fairing Configurations to Reduce Helicopter Drag," NASA TM 4540, 1993.

[5]Lachmann, G.V., Boundary Layer and Flow Control, Vol. 1, Pergamon Press, 1961.

[6]Greenblatt, D., Wygnanski, I., "The Control of Flow Separation by Periodic Excitation", *Progress in Aerospace Sciences*, Vol. 36, pp. 487-545, 2000.

[7]Jacot, D., Mabe, J., "Boeing Active Flow Control system for the V-22", AIAA Paper 2000-2473, *Fluids 2000*, Denver, CO, June 2000.

[8]Grife, R., Darabi, A., and Wygnanski, I. J., "Download Reduction on a Three Dimensional V-22 Model Using Active Flow Control", AIAA 2000-3071, 1st Flow Control Conference, St.Louis, MO, June 2002.

[9]McCormick D.C., "Boundary Layer Separation Control With Directed Synthetic Jets", AIAA Paper 2000-0519, 38th Aerospace Sciences Meeting Exhibit, Reno, NV, January 10-13, 2000.

[10]Simpson, R.L., Chew, Y.T., Shivaprasad, B.G., "The Structure of a Separating Turbulent Boundary Layer Part 1. Mean Flow and Reynolds Stresses", *Journal of Fluid Mechanics*, Vol. 113, pp. 23-51, March 1981.

[11]Smith, D.R., "Interaction Of A Synthetic Jet With A Crossflow Boundary Layer", *AIAA Journal*, Vol. 40, No. 11, November, 2002.

[12]White, F.M, Viscous Fluid Flow, McGraw-Hill, U.S.A, 1991.

[13]Brunn, H.H., Hot-Wire Anemometry: Principles and Signal Analysis, Oxford University Press, New York, 1995.

[14]Coleman, H.W, Steele, W.G, Experimentation and Uncertainty Analysis for Engineers, John Wiley Sons, U.S.A, 1999.

Table 1 Test cases and conditions.

Slot Configuration	Pressure Distribution	X-Wire Flow Survey	Near Field Survey
Baseline	No AFC ($\alpha = 0, 5$ and 10 deg)	No AFC	No AFC
$x/c = 0.30$ Slot	With AFC	With AFC	With AFC
$x/c = 0.30$ and 0.60 Slot	With AFC	With AFC	

[a] $Re = 1.0 \times 10^6$, $f = 120$ Hz, $\alpha = 10$ deg, With AFC: $C_\mu = 0.86\%$

Table 2 Integrated pressure force coefficients.

Slot Configuration	C_l	C_d	C_n	C_a
Baseline	-.141	.079	-.125	.102
$x/c = 0.30$ Slot	.104	.073	.115	.054
$x/c = 0.30$ and 0.60 Slot	.359	.068	.366	.004

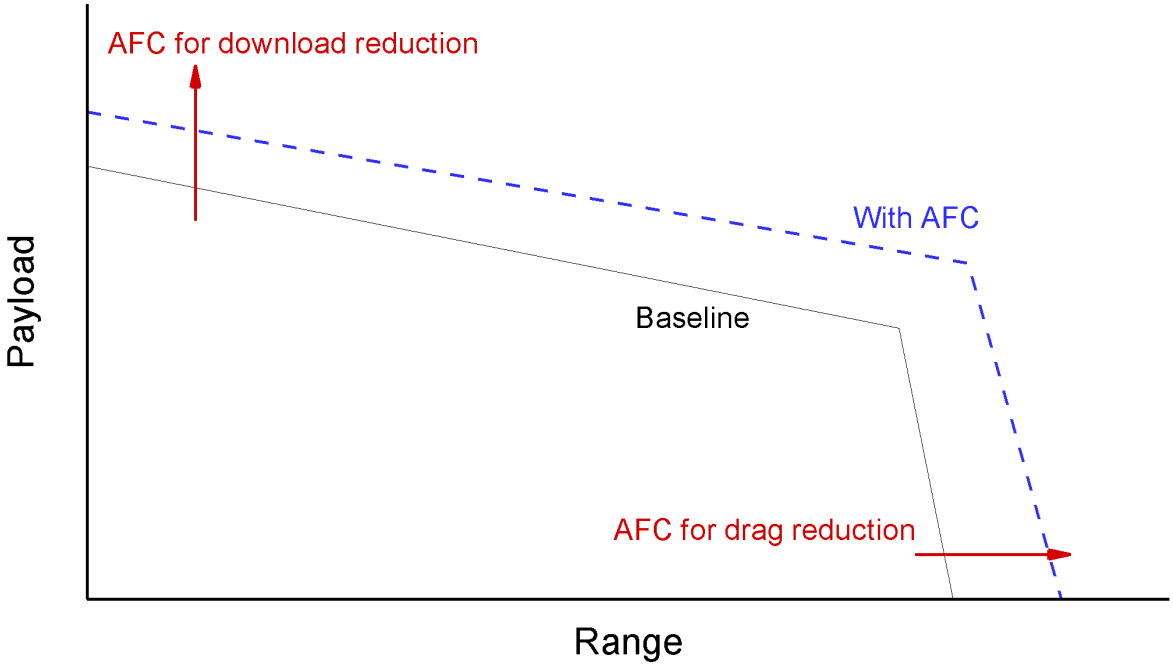

Fig. 1 Conceptual plot of potential performance increase.

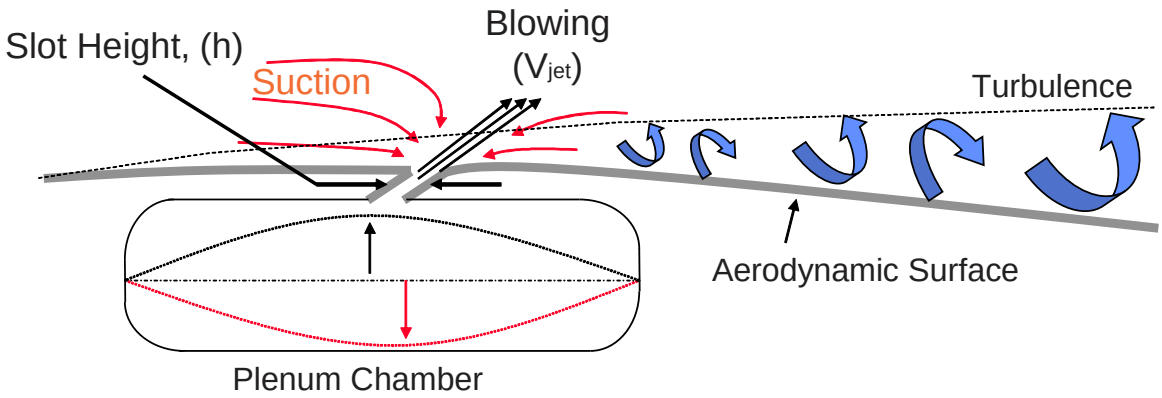

Fig. 2 Conceptual diagram of synthetic jet actuator.

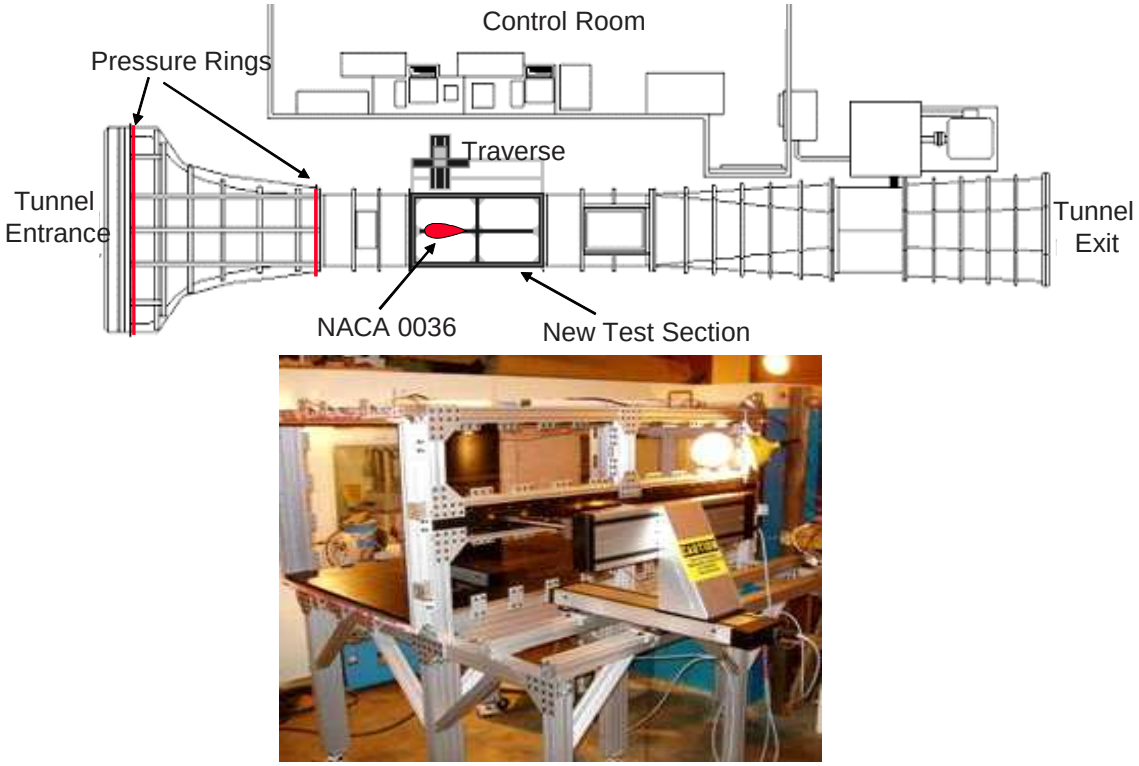

Fig. 3 CPSU 3-ft by 4-ft Wind Tunnel with new flow survey test section.

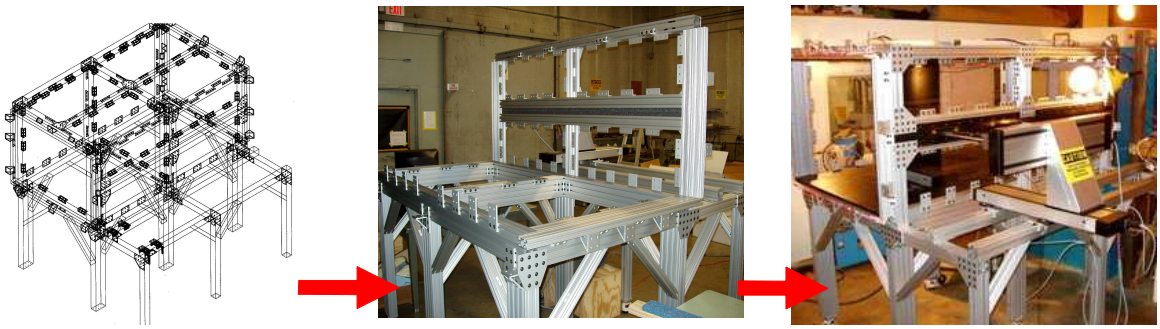

Fig. 4 Construction phases of flow survey test section.

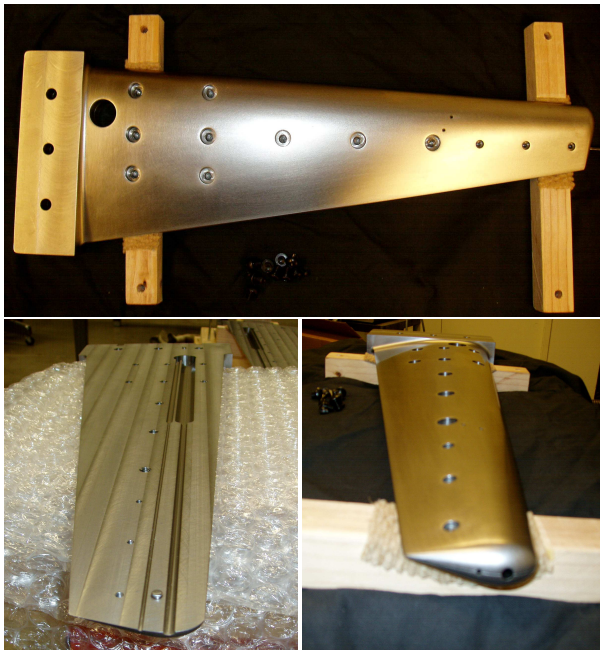

Fig. 5 Low vibration hot-wire probe support.

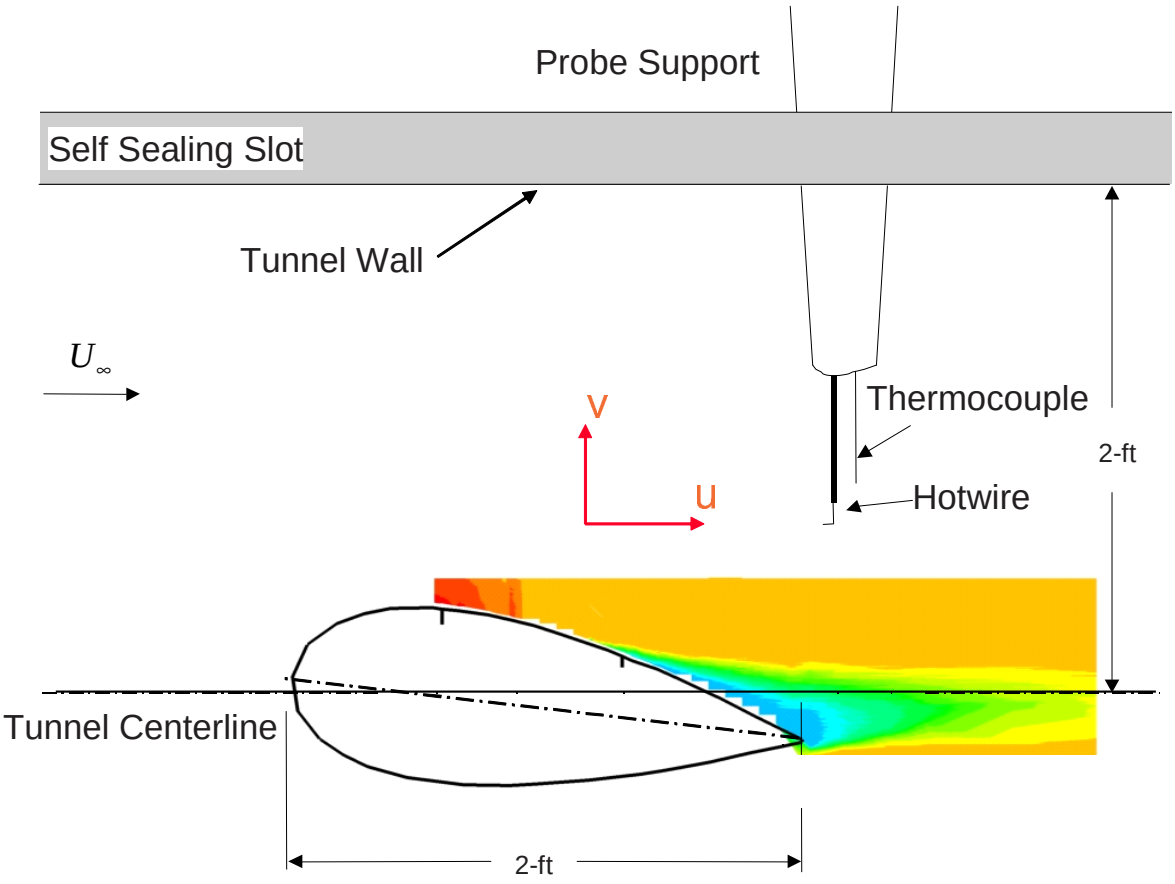

Fig. 6 Cross section diagram of test setup.

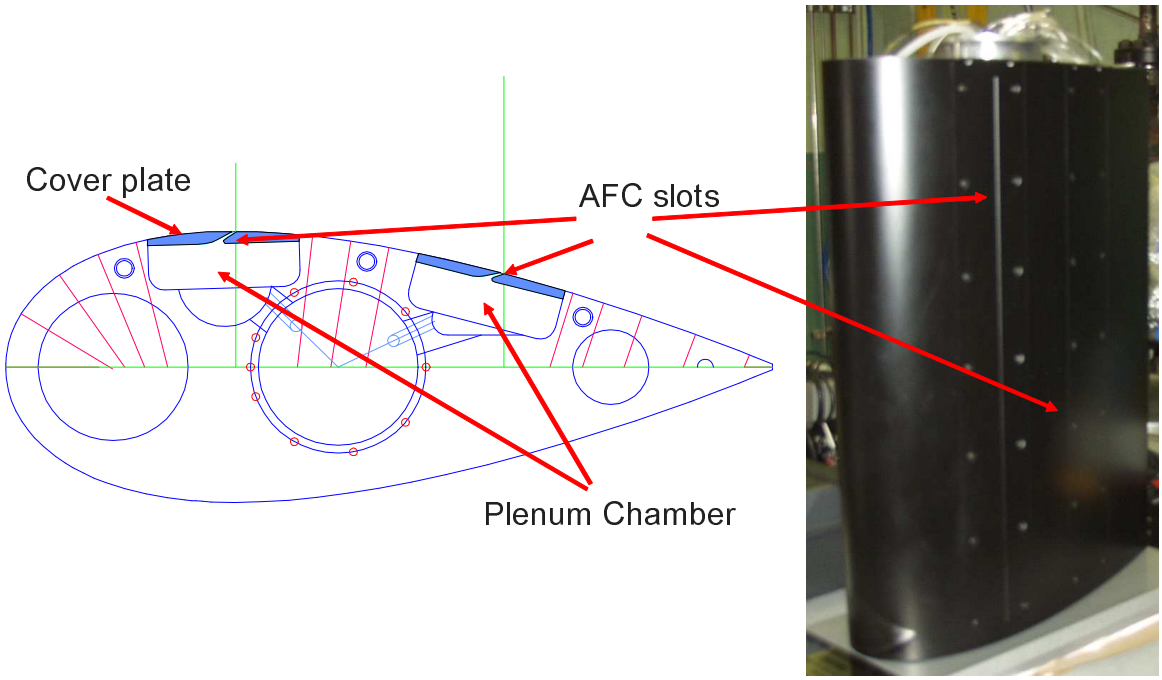

Fig. 7 NACA 0036 active flow control model.

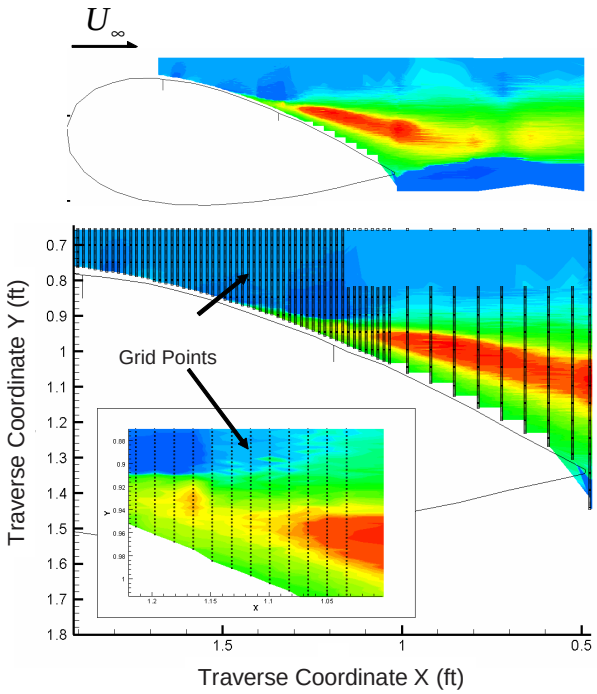

Fig. 8 Example x-wire survey grid.

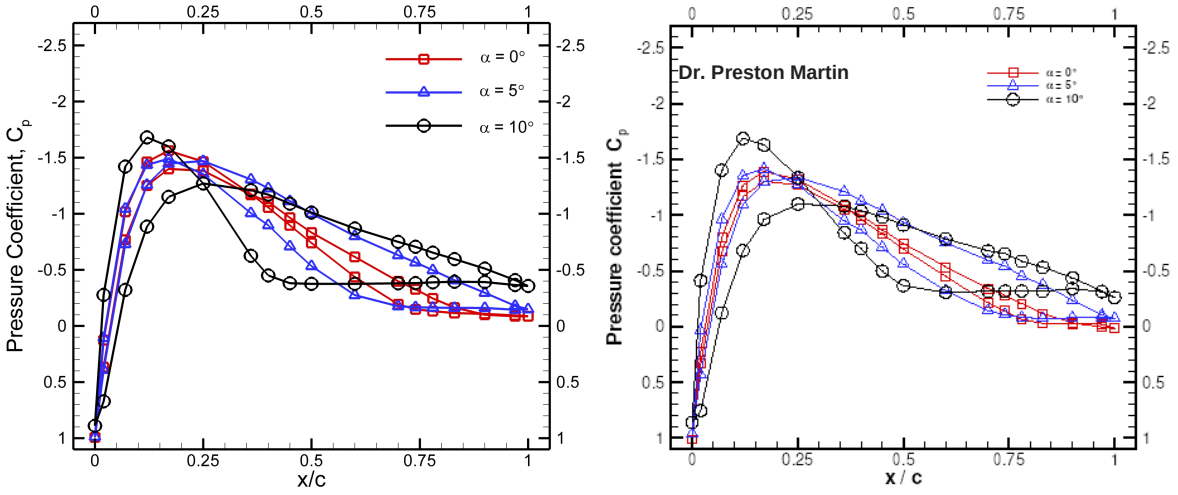

Fig. 9 Comparison of current and previous baseline pressure distributions. ($\alpha = 0$, 5, **and** 10 **deg**)

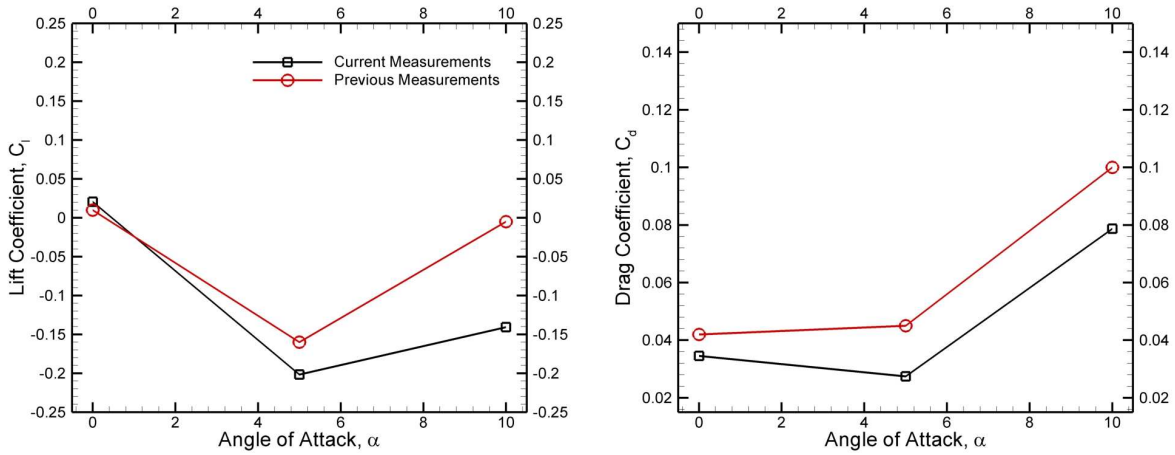

Fig. 10 Comparison of current and previous baseline integrated lift and drag. ($\alpha = 0$, 5, **and** 10 **deg**)

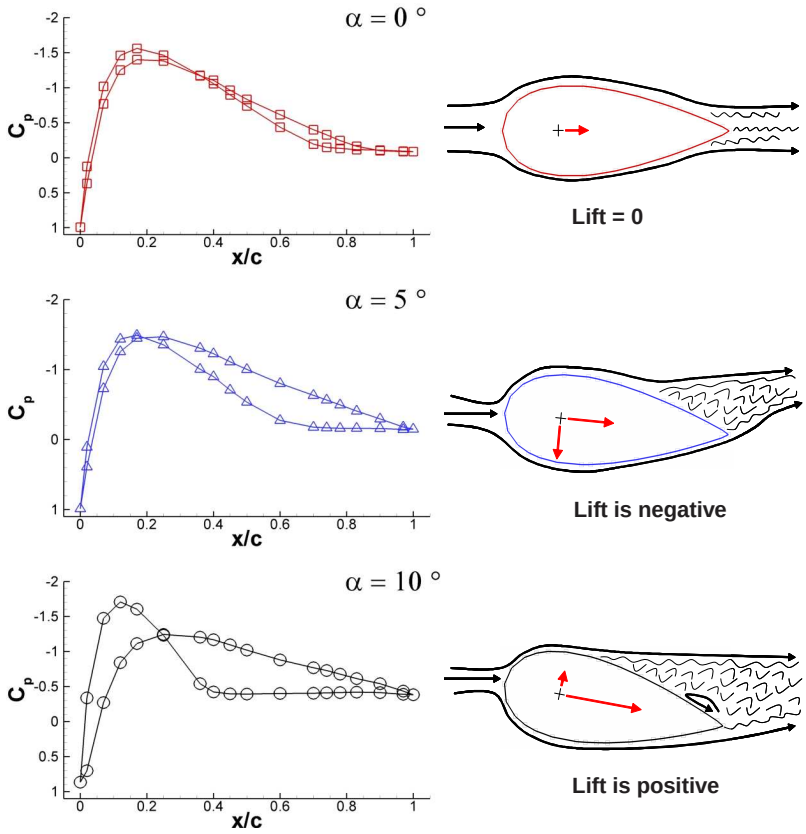

Fig. 11 Baseline pressure distributions and conceptual sketches illustrating lift reversal.

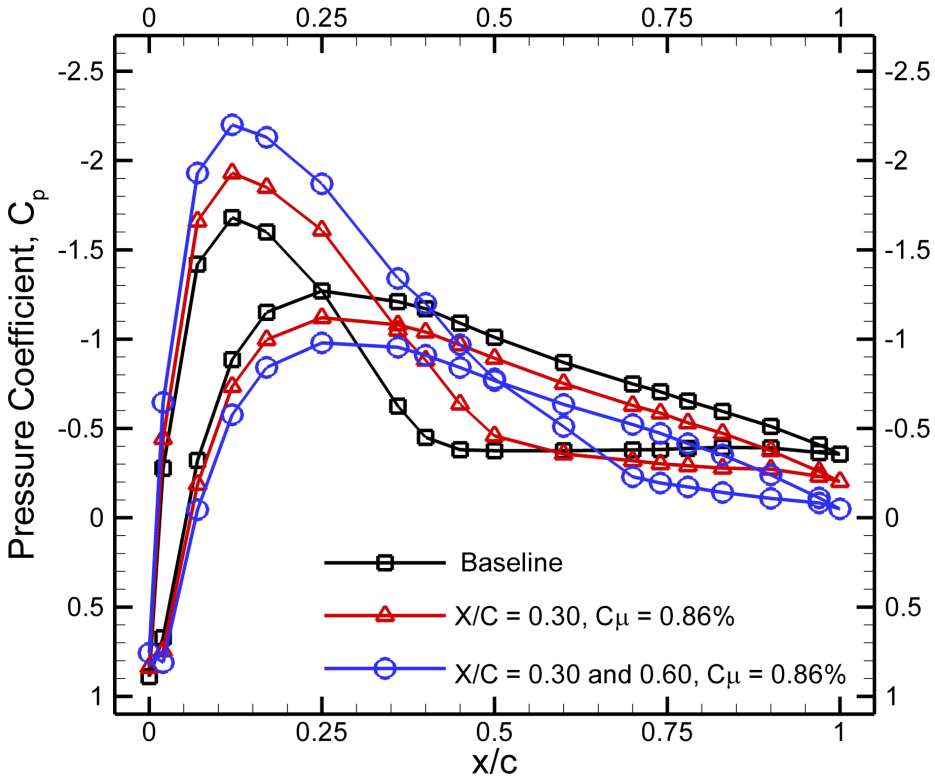

Fig. 12 Pressure distributions ($\alpha = 10$ deg) with different flow control slot configurations.

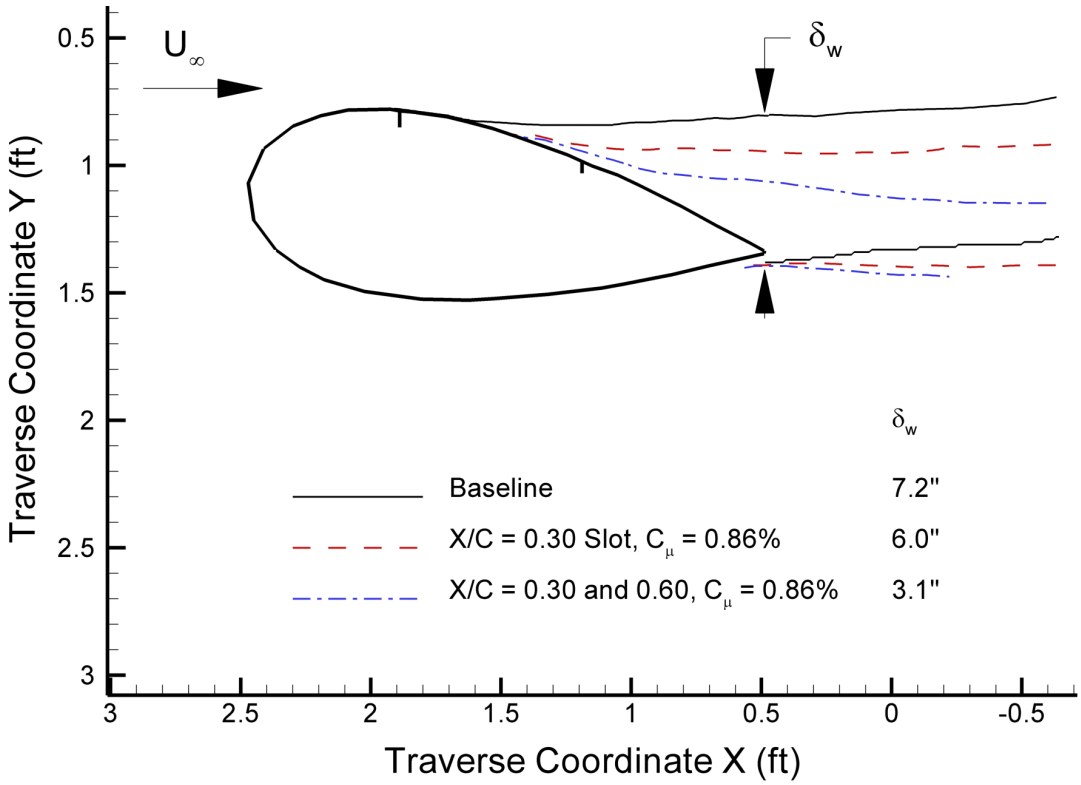

Fig. 13 Shear layer and wake comparison from x-wire flow survey.

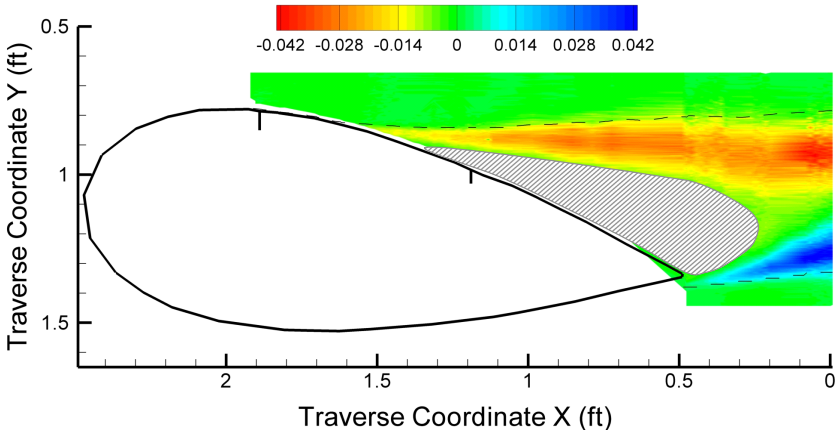

Fig. 14 Non-dimensional Reynolds shear stress contours. (Baseline)

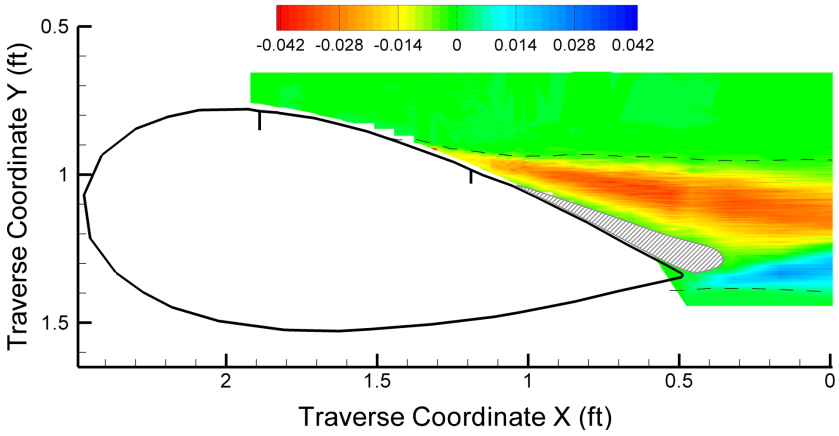

Fig. 15 Non-dimensional Reynolds shear stress contours. ($x/c = 0.30$ slot, $C_\mu = 0.86\%$).

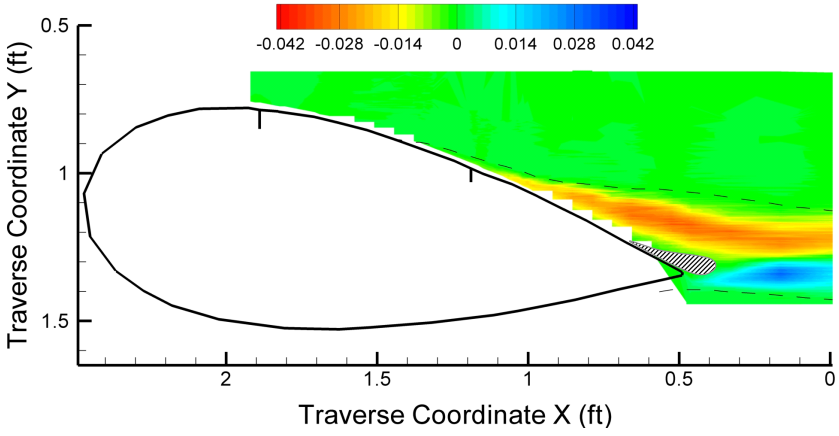

Fig. 16 Non-dimensional Reynolds shear stress contours. ($x/c = 0.65$ slot, $C_\mu = 0.86\%$).

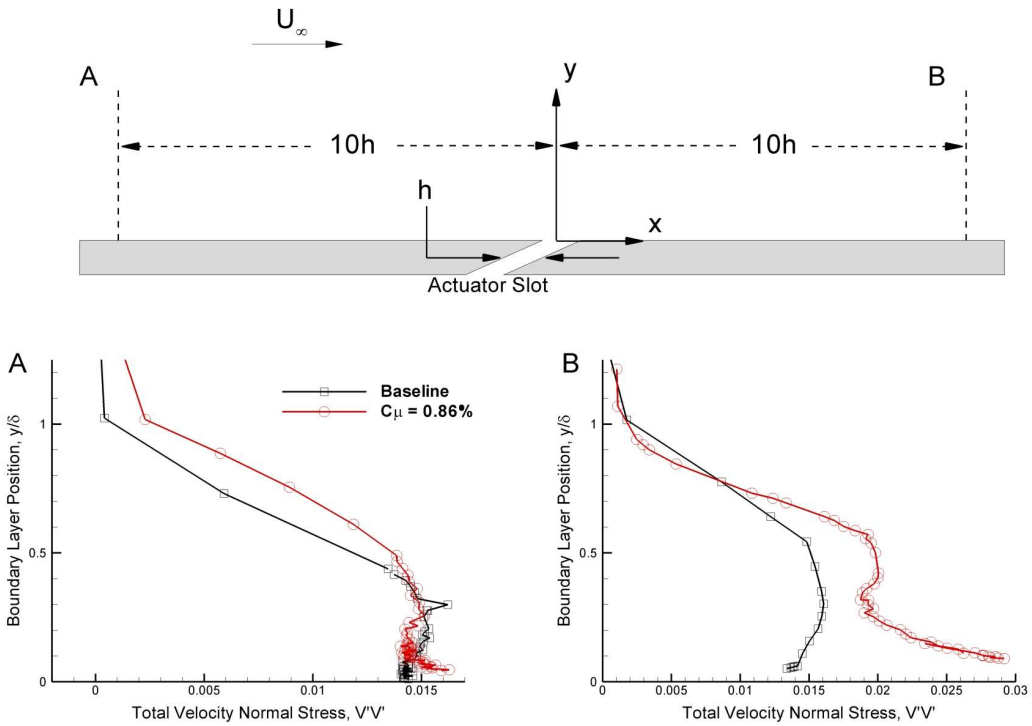

Fig. 17 Total velocity normal stress near x/c = 0.30 slot.